Ultramicroscopy 233 (2022) 113392

Contents lists available at ScienceDirect

Ultramicroscopy

journal homepage: www.elsevier.com/locate/ultramic

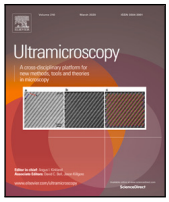

Continuous illumination picosecond imaging using a delay line detector in a transmission electron microscope

Teresa Weßels [a,b,*], Simon Däster [c], Yoshie Murooka [a], Benjamin Zingsem [d], Vadim Migunov [a,e], Maximilian Kruth [a], Simone Finizio [f], Peng-Han Lu [a], András Kovács [a], Andreas Oelsner [g], Knut Müller-Caspary [a,h], Yves Acremann [c], Rafal E. Dunin-Borkowski [a]

[a] Ernst Ruska-Centre for Microscopy and Spectroscopy with Electrons and Peter Grünberg Institute, Forschungszentrum Jülich, 52425 Jülich, Germany
[b] Lehrstuhl für Experimentalphysik IV E, RWTH Aachen University, 52056 Aachen, Germany
[c] Laboratory for Solid State Physics, ETH Zurich, 8093 Zurich, Switzerland
[d] Faculty of Physics and Center for Nanointegration (CENIDE), University of Duisburg–Essen, 47057 Duisburg, Germany
[e] Central Facility for Electron Microscopy (GFE), RWTH Aachen University, 52074 Aachen, Germany
[f] Swiss Light Source, Paul Scherrer Institut, 5232 Villigen PSI, Switzerland
[g] Surface Concept GmbH, 55124 Mainz, Germany
[h] Department of Chemistry, Ludwig-Maximilians-Universität München, Butenandtstrasse 5-13, 81377 Munich, Germany

ARTICLE INFO

Keywords:
Imaging techniques
Time-resolved transmission electron microscopy
Ferromagnetism
Lorentz microscopy

ABSTRACT

Progress towards analysing transitions between steady states demands improvements in time-resolved imaging, both for fundamental research and for applications in information technology. Transmission electron microscopy is a powerful technique for investigating the atomic structure, chemical composition and electromagnetic properties of materials with high spatial resolution and precision. However, the extraction of information about dynamic processes in the ps time regime is often not possible without extensive modification to the instrument while requiring careful control of the operation conditions to not compromise the beam quality. Here, we avoid these drawbacks by combining a delay line detector with continuous illumination in a transmission electron microscope. We visualize the gyration of a magnetic vortex core in real space and show that magnetization dynamics up to frequencies of 2.3 GHz can be resolved with down to ~122 ps temporal resolution by studying the interaction of an electron beam with a microwave magnetic field. In the future, this approach promises to provide access to resonant dynamics by combining high spatial resolution with sub-ns temporal resolution.

1. Introduction

The ability to study magnetization dynamics on the nm scale is of great importance for both nanoelectronics and fundamental science. Developments such as racetrack memories [1], information transport by spin waves [2], the use of magnetic vortices as radio frequency sources [3] and the use of magnetic-vortex-based spin torque nano-oscillators as dynamic sensors [4] emphasize the importance of magnetization dynamics in future applications. Current methods of time-resolved magnetic imaging, such as those based on synchrotron X-rays [5,6] and scanning electron microscopy with polarization analysis [7], allow the timescales of magneto-dynamic processes to be accessed through pump–probe imaging.

Magnetic imaging techniques based on transmission electron microscopy (TEM), such as Lorentz microscopy and off-axis electron holography, provide nm spatial resolution, even with the sample located in magnetic-field-free conditions [8,9], while offering complementary insight into the local microstructure and composition of the material [10]. However, the timescales of, *e.g.*, magnetic dynamics governed by the Landau–Lifshitz–Gilbert (LLG) equation, are on the order of 1 ps – 1 ns [11]. Whereas MHz and GHz resonances can be studied using X-rays with a typical spatial resolution of between 10 and 30 nm [12,13], the temporal resolution of most conventional TEM techniques that are based on continuous illumination is currently in the ms range and hence six orders of magnitudes too low. Pump–probe TEM techniques based on the use of laser-driven photo-cathodes offer temporal resolutions down to the sub-picosecond [14–17]. However, they require extensive modification to the gun system of the microscope,

* Corresponding author at: Ernst Ruska-Centre for Microscopy and Spectroscopy with Electrons and Peter Grünberg Institute, Forschungszentrum Jülich, 52425 Jülich, Germany.
E-mail address: t.wessels@fz-juelich.de (T. Weßels).

https://doi.org/10.1016/j.ultramic.2021.113392
Received 28 June 2021; Received in revised form 4 September 2021; Accepted 9 September 2021
Available online 14 October 2021

such as the introduction of a laser system. In addition, careful control of the operation conditions is vital to not compromise the electron beam quality.

Here, we report a proof-of-principle study that demonstrates real-time ps observation of the gyration of a magnetic vortex core in a ferromagnetic thin film using a delay line detector (DLD) mounted on a spherical aberration corrected transmission electron microscope. A DLD is a high sensitivity, fast detector that has been used for imaging and spectroscopy over several decades in various scientific fields [18], but has only rarely been applied in electron microscopy. Recently, it has been employed for coincidence experiments correlating electron energy-loss spectroscopy and energy dispersive X-ray spectroscopy [19]. The experiments that we describe below, which involve imaging a magnetic vortex core and electron diffraction, demonstrate a temporal resolution close to 100 ps and the ability to measure a beam deflection at a frequency of up to 2.3 GHz. We apply an in-plane magnetic field to a sample in the TEM by using a waveguide integrated in a single tilt TEM specimen holder, which can be operated over a frequency range of between DC and 40 GHz [20]. Our setup does not require any major modifications to the electron microscope, allowing electron beam coherence and spatial resolution to be maintained in both conventional and magnetic-field-free (Lorentz) imaging and diffraction. Moreover, the illumination is continuous and no pulsing is required to access magnetization dynamics.

2. Experimental details

The experimental setup is shown in Fig. 1. The sample is examined in an FEI Titan G2 60–300 TEM (300 kV), which is equipped with an objective lens aberration corrector and a Gatan Tridiem 865 ER imaging filter [21]. The objective lens is turned off and a non-immersion Lorentz lens, which is situated below the sample, is used to provide the magnetic-field-free imaging conditions that are required to investigate magnetic vortex states. The conventional microscope objective lens is then used to apply out-of-plane, static magnetic fields to the sample. The sample studied here consists of a permalloy [(Py), $Ni_{81}Fe_{19}$ alloy] disk that has a thickness of 130 nm and a diameter of 1.68 μm and is patterned using electron beam lithography onto a 20 nm thick SiN membrane. Details about the patterning process are given in Ref. [22]. The disk was transferred in a focused ion beam workstation onto a chip that is compatible with a radio frequency (RF) specimen holder. As a result of the geometry and dimensions of the Py disk, it supports a magnetic vortex state with an out-of-plane core.

The magnetic vortex core was excited into motion about its equilibrium configuration with an in-plane RF magnetic field, as described in Section 3.1 below. The RF generators (HP 8657B and HP 8671B) covered a frequency range of 100 MHz to 4 GHz. An amplifier (SPIN PA 233B A) was used to increase the RF current for all frequencies except for 100 MHz, with a total applied power of ∼20 dBm. In order to obtain temporal resolution, a frequency divider (developed in-house [23]) after the amplifier was used to divide the RF frequency by 64 to generate the starting signal of the DLD.

The DLD, which was provided by Surface Concept (single-anode delay line detector DLD4040) [18], was used to measure the positions and arrival times (x, y, t) of detected electrons, where t is the arrival time of each electron relative to an electronic starting signal. The DLD consists of a micro-channel plate (MCP), which generates a burst of secondary electrons for each detected primary electron. This burst is converted into a voltage pulse when it impacts an anode behind the MCP. In case of a delayline detector, the anode consists of two stacked meandering waveguides, oriented perpendicular to each other. The electron burst from the MCP generates two voltage pulses on each meander, which propagate in opposite direction towards the detection electronics. By measuring the difference in arrival time at the ends of the meanders one can determine the position of the detected electron. The time measurement is performed by a time-to-digital converter (TDC). The average arrival time provides the arrival time of the electron. Therefore, a DLD provides three-dimensional information (x, y, t).

The TDC measures the arrival time of each electron in steps of $\tau = 6.858711$ ps after the starting signal. The measured number of time steps $t_n = t/\tau$ was mapped onto one period of the RF signal by using a modulus operation, in the form of the number of time steps per RF period

$$m = \frac{1}{f_{RF}\tau} \quad , \tag{1}$$

where f_{RF} is the RF frequency. The resulting phase is $p_n = t_n \bmod m$ in units $\frac{2\pi}{m}$. The arrival time of the electron is assigned to the corresponding phase of the RF excitation. The individual electron events are binned into a three-dimensional dataset (x, y, p_n). As this procedure only works if m is a natural number, the RF frequency must be quantized as

$$f_{\mathrm{RF}} = \frac{1}{\tau k} \text{ with } k \in \mathbb{N}. \tag{2}$$

The position of the DLD behind the energy filter offers several advantages: (i) The energy filter can be used to filter out contributions due to inelastic scattering such as valence core losses. Moreover, it would be possible to image processes at specific energy levels. (ii) It is possible to achieve higher magnifications. (iii) When other external stimuli like lasers are employed, illumination of the detector with laser light can be avoided.

3. Results and discussion

3.1. Magnetic vortex core dynamics

The application of the DLD to time-resolved measurements was demonstrated by studying the real space motion of a magnetic vortex in a Py disk illuminated by a parallel electron beam. Magnetic vortices are ideal structures for such studies as a result of their simple geometry, stability and resonant dynamics [24–27]. In the present study, the magnetic vortex core was imaged in Lorentz mode using Fresnel defocus imaging (see Fig. 2(a)). The in-plane field of the magnetic vortex shown in Fig. 2(b) results in convergence of the electron beam due to the Lorentz force in an overfocus image. The magnetic vortex core was excited by using in-plane magnetic fields oscillating at microwave frequencies. In general, it is expected to follow an elliptical orbit at resonance, with its trajectory depending on the shape, size and material of the disk [28,29].

Fig. 2(c) shows real space snapshots of the motion of the magnetic vortex core at different phases of the excitation cycle for a frequency of ∼417 MHz, a power of 23 dBm and a static out-of-plane magnetic field of 18 mT. The applied power results in a magnetic field strength of ∼0.07 mT at the sample (see Supplementary Material for details). The parameters were chosen to maximize the motion of the magnetic vortex core, while being small enough to avoid switching of the core, which has been demonstrated to only require small in-plane fields [12]. A total integration time of 2 minutes was sufficient to resolve the full gyration, with individual snapshots corresponding to average time steps of 13 ps each. The background was removed by dividing each frame by an image without the sample after normalizing the counts to the total exposure time. Due to the defocus, the standard calibration of the DLD cannot be used. Hence, the conversion factor from pixels to nm is determined by measuring the size of the vortex core for several frequencies off-resonance and correlating it to a measurement of the core with a K2 detector and a known calibration. This method to calibrate the detector introduces an uncertainty of about 10% in the spatial domain. The snapshots reveal that the bright spot, which corresponds to the position of the magnetic vortex core, is displaced between successive phases of the excitation cycle and follows a clockwise trajectory. The position of the magnetic vortex core at each step of the excitation cycle was determined by finding the centre of mass of the brightest

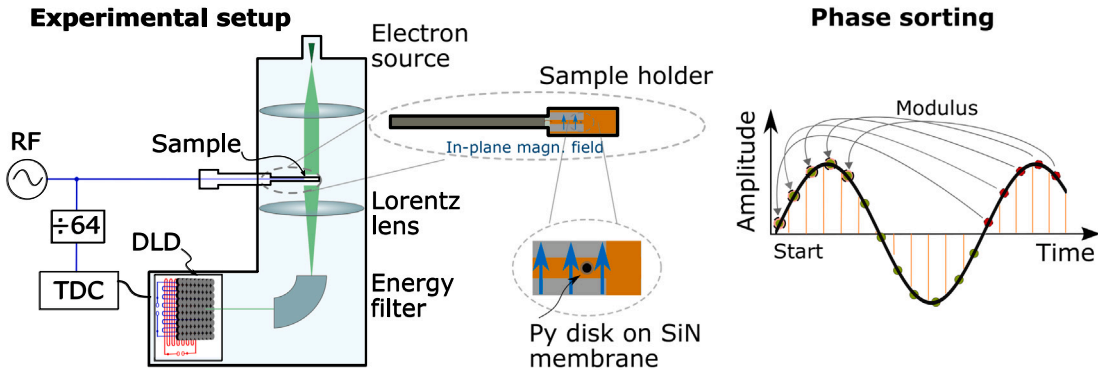

Fig. 1. Schematic diagram of the measurement setup and time binning used in the present study. (Left) The electron beam is deflected by a magnetic vortex core in a permalloy (Py) sample and imaged using a small area on the delay line detector (DLD). Two meanders on the detector record the times and positions of incoming electrons. Excitation of the magnetic vortex core and detection using the DLD are synchronized by using a frequency divider. (Right) The excitation cycle is divided into multiple steps. Steps corresponding to the same phase are summed up.

pixels. Its trajectory was recorded at several frequencies close to the frequency for which the displacement was greatest. The left plot in Fig. 2(d) shows the apparent position of the magnetic vortex core during a full excitation cycle for all frequencies. Technical limitations resulting in a distortion of the recorded image are compensated by applying the Brown–Conrady model [30] (see Supplementary Material for details). In addition to the vortex core motion, the position depends on the interaction of the electron beam with the microwave magnetic field, which results in a shift of the complete image. The image shift can be described approximately as a frequency-dependent sinusoidal deflection (see Supplementary Material for details). The true position of the magnetic vortex core was obtained by subtracting the image shift from the total deflection. The dependence of the resulting magnetic vortex core motion on applied frequency is shown in the right plot in Fig. 2(d). There is a sharp resonance between 417 and 419 MHz, with the magnetic vortex core motion then following an elliptical trajectory. There, the deflection of the vortex core corresponds to about 23 ± 3 nm in the x direction. Based on the elliptical trajectory, it can be excluded that the measured motion is purely an effect of the electron beam interaction with the RF fields as the latter would result in a linear deflection (see Supplementary Material for details).

The experimental results were compared with simulations based on the LLG equation obtained using MuMax^3 software [31,32]. The simulations were performed for a disk with a diameter of $d = 1.675\,\mu$m and a thickness of $t = 160$ nm, an exchange stiffness of $A_{ex} = 1.32 \cdot 10^{11}\,\frac{\mathrm{J}}{\mathrm{m}}$, a saturation magnetization of $M_S = 8 \cdot 10^5\,\frac{A}{m}$, a g-factor of $\gamma_{LL} = 2.1 \cdot \frac{\mu_B}{\hbar}$, a damping coefficient of $\alpha = 0.016$, an applied out-of-plane magnetic field of 20 mT and an in-plane oscillating magnetic field with an amplitude of 0.1 mT. Fig. 3 shows the results of the simulations, which reveal a sharp resonant frequency at 400 MHz, in good agreement with the experimental results. The inset to Fig. 3 shows the simulated trajectory of the magnetic vortex core in the disk. The transient period of a few ns that the magnetic vortex core requires to reach a stationary resonant trajectory is not included in the figure. The simulations reveal a slightly elliptical trajectory with a diameter of around 20 nm. This diameter is in good agreement with the experimental measured deflection in the x direction. Discrepancies in the shape of the trajectories between the simulations and experimental results may result from inadequate correction for the electron beam–electromagnetic field interaction in the experiment, which does not take the frequency-dependent formation of standing waves in the holder into account. Moreover, the microwave field may not have the properties expected for an ideal waveguide [33]. In future experiments, these factors can be separated from the vortex core motion, *e.g.*, by imaging the deflection of a non-magnetic marker structure under microwave excitation and subsequently subtracting it from the vortex core motion. Overall, the comparison between the simulations and the experimental results confirms that dynamics occurring on a length scale of a few tens of nm are accessible using the DLD, while retaining the imaging capabilities of the TEM.

3.2. Temporal resolution

Further prospects of combining a DLD with a TEM were investigated by determining the highest frequency that can be applied during imaging and the temporal resolution of the setup. For this purpose, the electron beam was positioned to illuminate only the SiN membrane and not the Py disk. The electron beam was then deflected only by its interaction with the microwave field introduced by the specimen holder *via* the Lorentz force. The deflection was imaged using low angle diffraction [34]. A high camera length of 115 m was used to compensate for the small deflection angle of 41 μrad and to concentrate the incident illumination onto a spot on the detector. The spot size of the beam on the detector was ~300 pixels^2. The deflection of the beam followed the phase of the excitation, with the spot undergoing sinusoidal motion parallel to the specimen holder axis. The total power of the excitation was chosen to be 17 dBm, which was sufficient to induce a resolvable deflection.

Fig. 4 shows the time-integrated trajectory of the electron beam for different applied frequencies. Data reduction was performed by combining varying numbers of frames for each phase into snapshots of 8 frames for 100 MHz and 2 frames for measurements between 500 MHz and 1.5 GHz. For higher frequencies, data reduction was not applied. After removing the background and a distortion correction (see Supplementary Material for details), all (x, y, p_n) datasets were smoothed using a Gaussian filter with $\sigma = 2$ pixels and rotated so that the primary axis of motion was parallel to the y axis. Each dataset was then cropped in the spatial domain to include only the deflected beam, as shown in Fig. 4. The sinusoidal motion can be seen in the time domain when summing over the x axis. The deflection does not follow the expected straight line, but is distorted. The bending of the deflections is thought to originate from remaining distortions of the recorded image (see Supplementary Material for details). The faint, dark lines at the bottom of the image integrated over the phase in Fig. 4a are a result of the distortion correction.

The highest resolvable frequency was determined by taking a linescan through the phase domain. The position of the linescan was chosen to be in the centre of the deflection. The highest resolvable frequency corresponds to the condition when two points of maximum deflection can be distinguished, *i.e.*, when two peaks are present in the linescan. The position of the linescans is marked by a red line in Fig. 4. Fig. 5(a) shows linescans for various frequencies. The condition that the two peaks need to be distinguishable is fulfilled up to ~2.314 GHz. The temporal resolution for the different frequencies is defined as the full width at half maximum (FWHM) of the linescans. Fig. 5(b) shows the FWHM of the broadest peak in the linescan for each frequency. The experimentally measured temporal resolution τ_{exp} is affected by the intrinsic temporal resolutions τ_i as well as the finite spot size of the

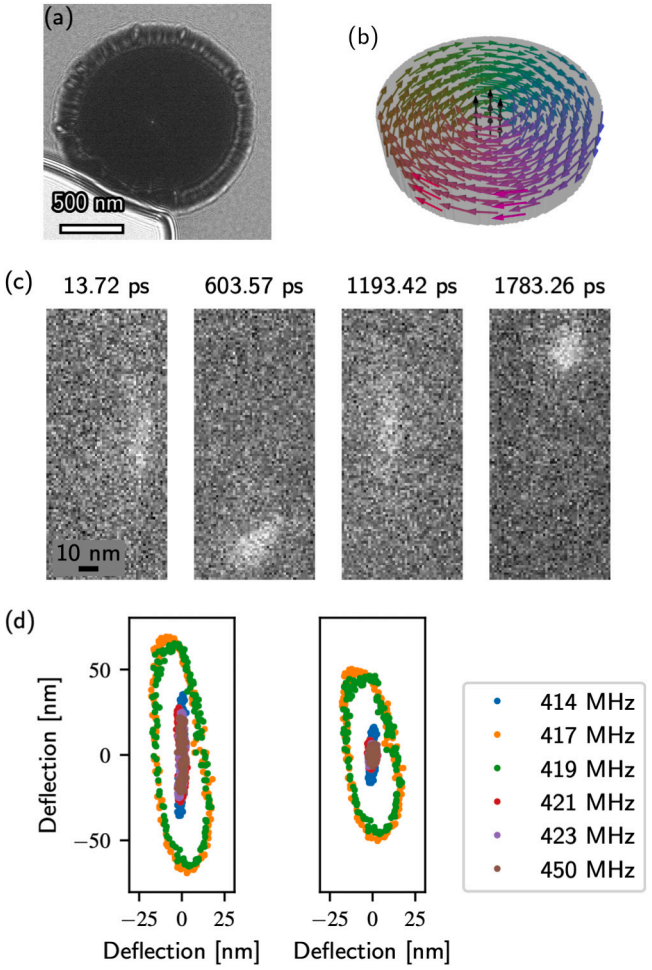

Fig. 2. Magnetic vortex core gyration. (a) Fresnel defocus image of a permalloy disk recorded in Lorentz mode at a defocus of 1 mm recorded with a K2 detector. The bright spot in the centre indicates the position of the vortex core. The bright region at the lower left edge is a cut in the supporting membrane. (b) Schematic image of a magnetic vortex state with clockwise rotation and a core pointing upwards. (c) Snapshots of magnetic vortex core motion recorded at different time steps over 13 ps during excitation at 417 MHz in an 18 mT static out-of-plane applied magnetic field. The images reveal clockwise motion of the magnetic vortex core. They have been binned by a factor of 4 in the x and y directions for better visibility. (d) Dependence of the position of magnetic vortex core in each frame on applied frequency, showing measurements before (left) and after (right) correction by subtraction of the image shift due to the electron beam–microwave interaction. The resonant frequency of the magnetic vortex core is characterized by an increase in the amplitude of the gyration at 417 and 419 MHz. The x and y axes have the same scaling.

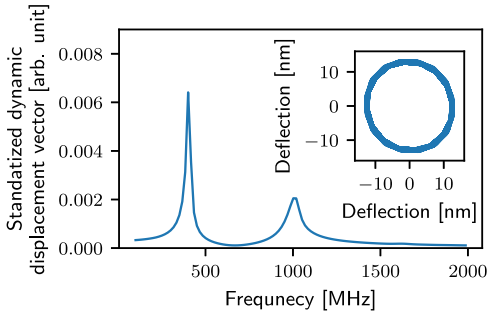

Fig. 3. Simulation of characteristics of magnetic vortex core dynamics, showing resonances at 400 and 1000 MHz. The stationary trajectory of the motion of the magnetic vortex core is shown in the inset for a frequency of 400 MHz.

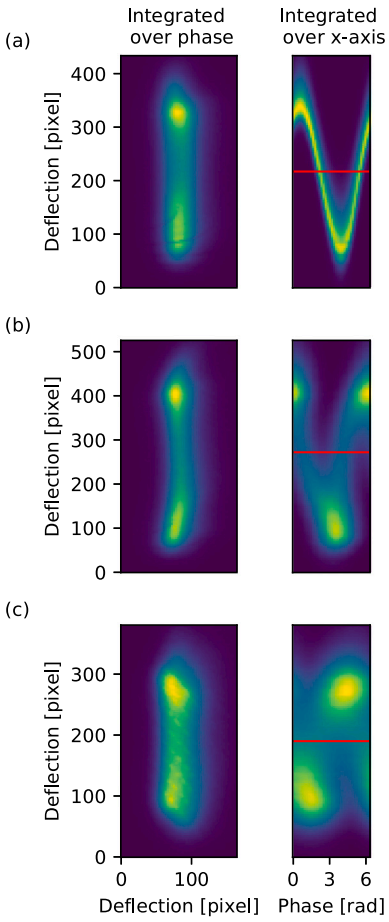

Fig. 4. Deflection of the electron beam by a microwave magnetic field visualized using low angle diffraction. The (x, y, p_n) datasets reveal sinusoidal motion for various frequencies: (a) ~0.1 GHz, (b) ~1.5 GHz and (c) ~2.5 GHz. Integration over the different phases and the x axis are shown in the left and right columns, respectively. The red line marks the position where a linescan was extracted.

electron beam τ_{spot}. In order to differentiate both effects, the sum of τ_i and τ_{spot} is fitted to τ_{exp}. Here, it is assumed that $\tau_{spot} = c/f_{RF}$ where c is constant. The intrinsic temporal resolution is as small as ~122 ps. The intrinsic temporal is limited by several factors: the time spread of the microchannel plate, the accuracy of the TDC as well as the jitter of the frequency divider. We optimized the frequency divider for low jitter; the estimate of the jitter from the used components in the signal path is around 5 ps. The main factor determining the intrinsic time resolution is likely the DLD. It consists of the resolution of the TDC (30 ps), amplitude-to-time conversion in the discriminators and the time spread of the microchannel plate. For the time spread, values ranging from 30 ps [35] up to 150 ps [36] are reported in the literature. DLDs of our type achieved 185 ps temporal resolution in photoelectron spectroscopy experiments [37].

The experiments performed in diffraction mode indicate that it is possible to perform dynamic measurements at frequencies of up to 2.3 GHz in the TEM using the present combination of a DLD and a microwave specimen holder with a temporal resolution of ~122 ps. This temporal resolution allows dynamic processes to be resolved up to the lower GHz regime.

3.3. Discussion

The results presented in this paper demonstrate the use of a DLD to provide access to temporal resolutions in the ps regime for a variety of dynamic processes, while making use of the full imaging potential

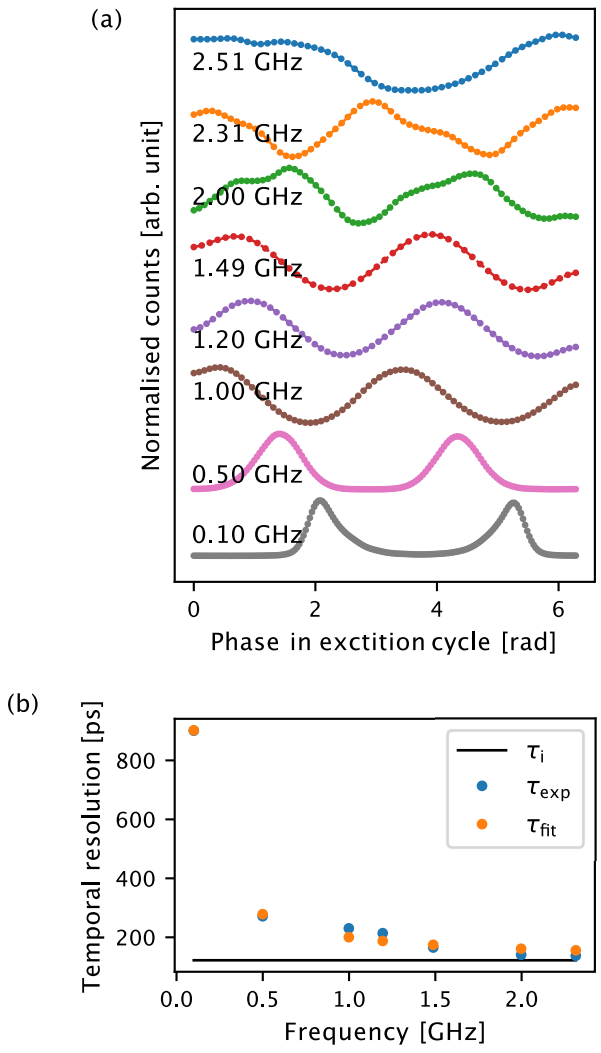

Fig. 5. Estimation of useable frequency range and temporal resolution. (a) Linescans recorded along the time domain of the integrated data over x for varying frequencies. Two peaks can be differentiated up to 2.3 GHz, suggesting that a sinusoidal motion is present and dynamic measurements can be performed up to this frequency. (b) FWHM τ_{exp} of the largest peak for the respective frequencies. τ_{fit} is a fit to τ_{exp} with contributions from τ_i and the effect of the spot size. The intrinsic spot size is ~122 ps.

of transmission electron microscopy. The technique is not limited to mapping magnetic properties, but can be applied in either real or diffraction space to studies of dynamic changes introduced by a variety of stimuli. The electronics of the DLD can be synchronized to different stimuli, such as lasers.

Although approaches based on ultrafast TEM provide access to various dynamic processes [16,38–41], they require a highly specialized or modified illumination system of the microscope. They may also compromise the quality of the electron beam, resulting in a low number of electrons per pulse [42] or beam displacement and blurring [43].

A key advantage of employing a DLD is the simplicity with which an existing microscope can be upgraded to achieve temporal resolution without the need for major modification and without compromising the quality of the electron beam or electron optics. It is only necessary to implement an additional camera or to exchange an existing one. In addition, the sample is imaged continuously, meaning that every electron can be recorded, thereby synchronized the electron dose and total measurement time. As the DLD is a single electron detection camera, the arrival time of each electron is measured. The technique is suited primarily to stroboscopic measurements to obtain sufficient contrast, just as for other ultrafast TEM approaches. The temporal resolution is currently limited to the ps regime as discussed in Section 3.2. Nevertheless, DLDs improve temporal resolution by six orders of magnitudes compared to most current TEM techniques. The benefit of the improved temporal resolution must be weighed against the degradation in terms of spatial resolution compared to these techniques. Nevertheless, the loss in terms of spatial resolution can be overcome by using higher magnifications at the cost of a reduced field of view. Therefore, a DLD can only be applied to experiments which do not require very good spatial resolution and large field of views at the same time. Other detectors, which aim towards ps temporal resolution, while maintaining a high electron dose and closing the gap in terms of spatial resolution, are under development confirming the high interest in improving temporal resolution in TEM measurements. One example is the Timepix 4 [44].

4. Conclusions

We have presented two proof-of-principle experiments, one in real space and one in diffraction space, which provide insight into the use of a delay line detector for time-resolved transmission electron microscopy. An external stimulus was provided by using a magnetizing specimen holder to introduce gyration of a magnetic vortex core and deflection of the electron beam. In real space, gyration of the magnetic vortex core was studied in terms of its resonance frequency, with resonance spectra resolved by imaging its motion. Low angle diffraction experiments showed that it is possible to image the deflection of the electron beam up to frequencies of 2.3 GHz, while achieving a temporal resolution down to ~122 ps. The full potential of this combination can be explored in future experiments by imaging other sample properties in the presence of different stimuli.

CRediT authorship contribution statement

Teresa Weßels: Conceived the project, Designed the experiments, Carried out the experiments, Analysed the experimental results, Prepared the manuscript, Discussed the results and commented on the manuscript. **Simon Däster:** Conceived the project, Designed the experiments, Carried out the experiments, Analysed the experimental results, Performed the micromagnetic simulations, Prepared the manuscript, Discussed the results and commented on the manuscript. **Yoshie Murooka:** Conceived the project, Designed the experiments, Carried out the experiments, Gave support for analysing the experimental results, Prepared the manuscript, Discussed the results and commented on the manuscript. **Benjamin Zingsem:** Conceived the project, Designed the experiments, Carried out the experiments, Performed the micromagnetic simulations, Discussed the results and commented on the manuscript. **Vadim Migunov:** Conceived the project, Designed the experiments, Carried out the experiments, Gave support for analysing the experimental results, Discussed the results and commented on the manuscript. **Maximilian Kruth:** Prepared the sample, Discussed the results and commented on the manuscript. **Simone Finizio:** Prepared the sample, Discussed the results and commented on the manuscript. **Peng-Han Lu:** Carried out the experiments, Discussed the results and commented on the manuscript. **András Kovács:** Gave support for analysing the experimental results, Prepared the manuscript, Discussed the results and commented on the manuscript. **Andreas Oelsner:** Conceived the project, Designed the experiments, Carried out the experiments, Discussed the results and commented on the manuscript. **Knut Müller-Caspary:** Conceived the project, Designed the experiments, Carried out the experiments, Prepared the manuscript, Discussed the results and commented on the manuscript. **Yves Acremann:** Conceived the project, Designed the experiments, Carried out the experiments, Gave support for analysing the experimental results, Prepared the manuscript, Discussed the results and commented on the manuscript. **Rafal E. Dunin-Borkowski:** Conceived the project, Designed the experiments, Prepared the manuscript, Discussed the results and commented on the manuscript.

Declaration of competing interest

The authors declare that they have no known competing financial interests or personal relationships that could have appeared to influence the work reported in this paper.

Acknowledgements

We are grateful to Werner Pieper, Alexander Clausen and Alexander Müller for help with instrumentation and to Thibaud Denneulin for supporting experiments. In addition, we thank Rolf Speen and Philipp Kükenbrink for technical help in developing the magnetizing holder and Ralf Meckenstock and Ulrich Poppe for helpful discussions. Furthermore, we acknowledge Michael Farle for helpul input and discussions. This work is supported by the Deutsche Forschungsgemeinschaft (DFG) through CRC/TRR 270 (Project ID 405553726), the European Union's Horizon 2020 Research and Innovation Programme (Grant No. 856538, project "3D MAGiC" and Grant No. 823717, project "ESTEEM3") and ETH Zurich. The authors are grateful for funding from the Innovation Pool for the Joint Laboratory for Model and Data Driven Material Characterization in the Helmholtz Association. K. M.-C. acknowledges funding from the Impuls and Vernetzungsfond under contract VH-NG-1317.

Appendix A. Supplementary data

Supplementary material related to this article can be found online at https://doi.org/10.1016/j.ultramic.2021.113392. See Supplementary Material for (1) videos of the vortex core gyration, (2) estimation of the microwave magnetic field, (3) interaction of the microwave field and the electron beam, and (4) image distortions.

References

[1] S. Parkin, M. Hayashi, L. Thomas, Magnetic domain-wall racetrack memory, Science 320 (5873) (2008) 190–194, http://dx.doi.org/10.1126/science.1145799.

[2] B.W. Zingsem, T. Feggeler, A. Terwey, S. Ghaisari, D. Spoddig, D. Faivre, R. Meckenstock, M. Farle, M. Winklhofer, Biologically encoded magnonics, Nature Commun. 10 (1) (2019) 1–8.

[3] S. Wintz, V. Tiberkevich, M. Weigand, J. Raabe, J. Lindner, A. Erbe, A. Slavin, J. Fassbender, Magnetic vortex cores as tunable spin-wave emitters, Nat. Nanotechnol. 11 (11) (2016) 948–953, http://dx.doi.org/10.1038/nnano.2016.117.

[4] A.S. Jenkins, L.S.E. Alvarez, P.P. Freitas, R. Ferreira, Digital and analogue modulation and demodulation scheme using vortex-based spin torque nano-oscillators, Sci. Rep. 10 (1) (2020) 1–7, http://dx.doi.org/10.1038/s41598-020-68001-6.

[5] P. Fischer, G. Denbeaux, T. Ono, T. Okuno, T. Eimüller, D. Goll, G. Schütz, Magnetic soft X-ray transmission microscopy, Curr. Opin. Solid State Mater. Sci. 7 (2) (2003) 173–179, http://dx.doi.org/10.1088/0022-3727/35/19/310.

[6] W. Chao, P. Fischer, T. Tyliszczak, S. Rekawa, E. Anderson, P. Naulleau, Real space soft x-ray imaging at 10 nm spatial resolution, Opt. Express 20 (9) (2012) 9777–9783, http://dx.doi.org/10.1364/OE.20.009777, URL http://www.opticsexpress.org/abstract.cfm?URI=oe-20-9-9777.

[7] R. Frömter, F. Kloodt, S. Rößler, A. Frauen, P. Staeck, D.R. Cavicchia, L. Bocklage, V. Röbisch, E. Quandt, H.P. Oepen, Time-resolved scanning electron microscopy with polarization analysis, Appl. Phys. Lett. 108 (14) (2016) 142401, http://dx.doi.org/10.1063/1.4945053.

[8] A. Kovács, R.E. Dunin-Borkowski, Magnetic imaging of nanostructures using off-axis electron holography, in: Handbook of Magnetic Materials, Vol. 27, Elsevier, 2018, pp. 59–153, http://dx.doi.org/10.1016/bs.hmm.2018.09.001.

[9] M. Krajnak, D. McGrouther, D. Maneuski, V. O'Shea, S. McVitie, Pixelated detectors and improved efficiency for magnetic imaging in STEM differential phase contrast, Ultramicroscopy 165 (2016) 42–50, http://dx.doi.org/10.1016/j.ultramic.2016.03.006.

[10] P.W. Hawkes, J. Spence, Springer Handbook of Microscopy, Springer Nature, 2019, http://dx.doi.org/10.1007/978-3-030-00069-1.

[11] S.J. Gamble, M.H. Burkhardt, A. Kashuba, R. Allenspach, S.S.P. Parkin, H.C. Siegmann, J. Stöhr, Electric field induced magnetic anisotropy in a ferromagnet, Phys. Rev. Lett. 102 (21) (2009) 217201, http://dx.doi.org/10.1103/PhysRevLett.102.217201.

[12] B. Van Waeyenberge, A. Puzic, H. Stoll, K. Chou, T. Tyliszczak, R. Hertel, M. Fähnle, H. Brückl, K. Rott, G. Reiss, et al., Magnetic vortex core reversal by excitation with short bursts of an alternating field, Nature 444 (7118) (2006) 461–464.

[13] X. Shi, P. Fischer, V. Neu, D. Elefant, J.C.T. Lee, D.A. Shapiro, M. Farmand, T. Tyliszczak, H.-W. Shiu, S. Marchesini, S. Roy, S.D. Kevan, Soft x-ray ptychography studies of nanoscale magnetic and structural correlations in thin SmCo5 films, Appl. Phys. Lett. 108 (9) (2016) 094103, http://dx.doi.org/10.1063/1.4942776.

[14] D.J. Flannigan, A.H. Zewail, 4D electron microscopy: Principles and applications, Acc. Chem. Res. 45 (10) (2012) 1828–1839.

[15] L. Piazza, D. Masiel, T. LaGrange, B. Reed, B. Barwick, F. Carbone, Design and implementation of a fs-resolved transmission electron microscope based on thermionic gun technology, Chem. Phys. 423 (2013) 79–84.

[16] A. Feist, N. Bach, N. Rubiano da Silva, T. Danz, M. Möller, K.E. Priebe, T. Domröse, J.G. Gatzmann, S. Rost, J. Schauss, et al., Ultrafast transmission electron microscopy using a laser-driven field emitter: Femtosecond resolution with a high coherence electron beam, Ultramicroscopy 176 (2017) 63–73, URL http://www.sciencedirect.com/science/article/pii/S0304399116303709.

[17] J. Yang, Y. Yoshida, H. Yasuda, Ultrafast electron microscopy with relativistic femtosecond electron pulses, Microscopy 67 (5) (2018) 291–295.

[18] A. Oelsner, O. Schmidt, M. Schicketanz, M. Klais, G. Schönhense, V. Mergel, O. Jagutzki, H. Schmidt-Böcking, Microspectroscopy and imaging using a delay line detector in time-of-flight photoemission microscopy, Rev. Sci. Instrum. 72 (10) (2001) 3968–3974, http://dx.doi.org/10.1063/1.1405781.

[19] D. Jannis, K. Müller-Caspary, A. Béché, A. Oelsner, J. Verbeeck, Spectroscopic coincidence experiments in transmission electron microscopy, Appl. Phys. Lett. 114 (14) (2019) 143101, http://dx.doi.org/10.1063/1.5092945, URL http://aip.scitation.org/doi/10.1063/1.5092945.

[20] B. Zingsem, Pico-second Spin Dynamics in Nano-Structures: Towards Nanometer Spatial Resolution by Transmission Electron Microscopy (Ph.D. thesis), Universität Duisburg-Essen, 2020.

[21] C. Boothroyd, A. Kovács, K. Tillmann, FEI titan G2 60–300 HOLO, J. Large-Scale Res. Facil. 2 (2016) 44, http://dx.doi.org/10.17815/jlsrf-2-70.

[22] S. Finizio, S. Wintz, D. Bracher, E. Kirk, A.S. Semisalova, J. Förster, K. Zeissler, T. Weßels, M. Weigand, K. Lenz, et al., Thick permalloy films for the imaging of spin texture dynamics in perpendicularly magnetized systems, Phys. Rev. B 98 (10) (2018) 104415.

[23] Frequency divider, https://github.com/eduphys/frequency-divider.

[24] S.-B. Choe, Y. Acremann, A. Scholl, A. Bauer, A. Doran, J. Stöhr, H.A. Padmore, Vortex core-driven magnetization dynamics, Science 304 (5669) (2004) 420–422, http://dx.doi.org/10.1126/science.1095068.

[25] R. Antos, Y. Otani, J. Shibata, Magnetic vortex dynamics, J. Phys. Soc. Japan 77 (3) (2008) 031004, http://dx.doi.org/10.1143/JPSJ.77.031004.

[26] N. Rubiano da Silva, M. Möller, A. Feist, H. Ulrichs, C. Ropers, S. Schäfer, Nanoscale mapping of ultrafast magnetization dynamics with femtosecond lorentz microscopy, Phys. Rev. X 8 (3) (2018) 031052, http://dx.doi.org/10.1103/PhysRevX.8.031052, URL https://link.aps.org/doi/10.1103/PhysRevX.8.031052.

[27] M. Möller, J.H. Gaida, S. Schäfer, C. Ropers, Few-nm tracking of current-driven magnetic vortex orbits using ultrafast Lorentz microscopy, Comm. Phys. 3 (1) (2020) 1–7, http://dx.doi.org/10.1038/s42005-020-0301-y, URL https://www.nature.com/articles/s42005-020-0301-y.

[28] K.Y. Guslienko, B. Ivanov, V. Novosad, Y. Otani, H. Shima, K. Fukamichi, Eigenfrequencies of vortex state excitations in magnetic submicron-size disks, J. Appl. Phys. 91 (10) (2002) 8037–8039, http://dx.doi.org/10.1063/1.1450816.

[29] V. Novosad, F.Y. Fradin, P.E. Roy, K.S. Buchanan, K.Y. Guslienko, S.D. Bader, Magnetic vortex resonance in patterned ferromagnetic dots, Phys. Rev. B 72 (2) (2005) 024455, http://dx.doi.org/10.1103/PhysRevB.72.024455.

[30] C. Brown, Close range camera calibration, Symposium on close range photogrammetry, Photogramm. Eng. Remote. Sens. 8 (1971) 855–866.

[31] A. Vansteenkiste, J. Leliaert, M. Dvornik, M. Helsen, F. Garcia-Sanchez, B. Van Waeyenberge, The design and verification of Mumax3, AIP Adv. 4 (10) (2014) 107133, http://dx.doi.org/10.1063/1.4899186.

[32] L. Exl, S. Bance, F. Reichel, T. Schrefl, H. Peter Stimming, N.J. Mauser, LaBonte's method revisited: An effective steepest descent method for micromagnetic energy minimization, J. Appl. Phys. 115 (17) (2014) 17D118, http://dx.doi.org/10.1063/1.4862839.

[33] D.M. Pozar, Microwave Engineering, John Wiley & Sons, 2011.

[34] F. Goncalves, G. Paterson, D. McGrouther, T. Drysdale, Y. Togawa, D. Schmool, R. Stamps, Probing microwave fields and enabling in-situ experiments in a transmission electron microscope, Sci. Rep. 7 (1) (2017) 1–6, http://dx.doi.org/10.1038/s41598-017-11009-2.

[35] D.A. Debrah, G.A. Stewart, G. Basnayake, A. Nomerotski, P. Svihra, S.K. Lee, W. Li, Developing a camera-based 3D momentum imaging system capable of 1 Mhits/s, Rev. Sci. Instrum. 91 (2) (2020) 023316, http://dx.doi.org/10.1063/1.5138731.

[36] M. Huth, C.-T. Chiang, A. Trützschler, F.O. Schumann, J. Kirschner, W. Widdra, Electron pair emission detected by time-of-flight spectrometers: Recent progress, Appl. Phys. Lett. 104 (6) (2014) 061602, http://dx.doi.org/10.1063/1.4864274.

[37] M.H. Berntsen, O. Götberg, O. Tjernberg, An experimental setup for high resolution 10.5 eV laser-based angle-resolved photoelectron spectroscopy using a time-of-flight electron analyzer, Rev. Sci. Instrum. 82 (9) (2011) 095113, http://dx.doi.org/10.1063/1.3637464.

[38] J.C. Williamson, J. Cao, H. Ihee, H. Frey, A.H. Zewail, Clocking transient chemical changes by ultrafast electron diffraction, Nature 386 (6621) (1997) 159–162, http://dx.doi.org/10.1038/386159a0.

[39] X. Fu, E. Wang, Y. Zhao, A. Liu, E. Montgomery, V.J. Gokhale, J.J. Gorman, C. Jing, J.W. Lau, Y. Zhu, Direct visualization of electromagnetic wave dynamics by laser-free ultrafast electron microscopy, Sci. Adv. 6 (40) (2020) eabc3456, http://dx.doi.org/10.1126/sciadv.abc3456, URL https://advances.sciencemag.org/content/6/40/eabc3456.

[40] J.W. Lau, K.B. Schliep, M.B. Katz, V.J. Gokhale, J.J. Gorman, C. Jing, A. Liu, Y. Zhao, E. Montgomery, H. Choe, et al., Laser-free GHz stroboscopic transmission electron microscope: Components, system integration, and practical considerations for pump–probe measurements, Rev. Sci. Instrum. 91 (2) (2020) 021301, http://dx.doi.org/10.1063/1.5131758.

[41] J. Van Rens, W. Verhoeven, E. Kieft, P. Mutsaers, O. Luiten, Dual mode microwave deflection cavities for ultrafast electron microscopy, Appl. Phys. Lett. 113 (16) (2018) 163104, http://dx.doi.org/10.1063/1.5049806.

[42] F. Houdellier, G. Caruso, S. Weber, M. Hÿtch, C. Gatel, A. Arbouet, Optimization of off-axis electron holography performed with femtosecond electron pulses, Ultramicroscopy 202 (2019) 26–32, http://dx.doi.org/10.1016/j.ultramic.2019.03.016.

[43] L. Zhang, M.W. Garming, J.P. Hoogenboom, P. Kruit, Beam displacement and blur caused by fast electron beam deflection, Ultramicroscopy 211 (2020) 112925, http://dx.doi.org/10.1016/j.ultramic.2019.112925.

[44] M. Campbell, J. Alozy, R. Ballabriga, E. Frojdh, E. Heijne, X. Llopart, T. Poikela, L. Tlustos, P. Valerio, W. Wong, Towards a new generation of pixel detector readout chips, J. Instrum. 11 (01) (2016) C01007, http://dx.doi.org/10.1088/1748-0221/11/01/c01007.